Deciphering Unexplored Reversible Potassium Storage and Small Volume Change in a CaV$_4$O$_9$ Anode with In Situ Transmission Electron Microscopy

Yi Wu, Peijie Wu, Yushu Tang, Ruining Fu, Yujie Cui, Jing Chen, Christian Kübel, and Feng Xu*

Vanadium-based compounds are explored as promising electrode materials in lithium/sodium-ion batteries exhibiting superior energy storage properties. However, similar attempts are rarely reported for potassium-ion batteries (PIBs), in which the fundamental reaction mechanisms remain inexplicit. Herein, porous CaV$_4$O$_9$ nanobelts (NBs) are selected as a PIB anode to systematically investigate potassium storage mechanisms through in situ transmission electron microscopy. In situ measurements track overall electrochemical potassiation reactions of CaV$_4$O$_9$ and identify a polyphase state of V$_4$O$_7$, CaO, and K$_2$O phases after potassiation. Unexpectedly, the potassiated products can be partially converted back to the original CaV$_4$O$_9$ phase with residual VO$_2$ and CaO phases, which is different from the irreversible phase transformations in lithium/sodium storages of CaV$_4$O$_9$. Impressively, the cavities in NBs alternately disappear and appear with (de)potassiation, avoiding the drastic volume change and structural degradation of anodes. The reversible potassium storage and stable cycling are evaluated by electrochemical measurements and in situ X-ray diffraction analysis. This work provides a paradigm by revisiting the existing anode materials in lithium/sodium-ion batteries to seek out viable anodes for next-generation PIBs.

Y. Wu, R. Fu, Y. Cui, J. Chen, F. Xu
SEU-FEI Nano-Pico Center
Key Laboratory of MEMS of the Ministry of Education
Southeast University
Nanjing 210096, China
E-mail: fxu@seu.edu.cn

Y. Wu, Y. Tang, C. Kübel
Institute of Nanotechnology
Karlsruhe Institute of Technology
Hermann-von-Helmholtz-Platz 1, 76344 Eggenstein-Leopoldshafen,
Germany

Y. Wu
School of Electromechanical Engineering
Guangdong University of Technology
Guangzhou 510006, China

P. Wu
State Key Laboratory of Advanced Technology for Materials Synthesis and Processing
Wuhan University of Technology
Wuhan 430070, China

1. Introduction

The rapidly growing markets of portable electronics and electric vehicles have created a strong demand for rechargeable batteries with high energy density and long cycling life.[1−3] However, the rarity of lithium in the earth's crust (only 0.0017 wt.%) and the increasing cost of lithium compounds hinder a wider usage of lithium-ion batteries (LIBs).[4−6] Sodium-ion batteries (SIBs)[7−9] and potassium-ion batteries (PIBs)[10−12] have attracted wide attention due to the comparatively high natural abundance and low cost of sodium and potassium resources. Compared with SIBs, PIBs have the advantage of a lower standard electrode potential (K$^+$/K: −2.93 V vs Na$^+$/Na: −2.71 V), which guarantees a higher operation voltage and energy density in batteries. Furthermore, among Li$^+$, Na$^+$, and K$^+$, the higher ionic conductivity and the lower desolvation energy of solvated K$^+$ enable the faster electrode reaction kinetics of PIBs.[13−16] Despite these merits, the larger ion size of K$^+$ (1.38 Å) inevitably results in rapid capacity decay and poor cycling stability, which becomes the main obstacle for the practical application of PIBs.[17−20] Therefore, the search for suitable electrode materials for PIBs with long-term cycling stability and high capacity is desired but challenging.

The prototype of potassium-based batteries employing a potassium anode was first reported by Ali Eftekhari.[21] After that, a series of anode materials have been attempted for use in PIBs, including conversion-type (e.g. VSe$_2$,[19] MoS$_2$,[22] and MnO$_2$[23]) and alloying-type (e.g. Sb,[24] P,[25] and Bi[26]) anodes. Nonetheless, their practical applicability in PIBs suffers from the low conductivity and the drastic volume change (such as ≈681% for Sn$_4$P$_3$[27]) during cycling. Different from the conventional conversion-type anodes, vanadium oxides potentially possess small volume change when used as anodes, since the valence of vanadium rarely reaches zero at low voltage due to the strong V−O bond strength.[28,29] Additionally, vanadium can achieve multi-electron transfer below 1.0 V due to its multivalent characteristics, indicating that it may deliver a higher theoretical capacity.[30] A case in point is the vanadium-based anode material, CaV$_4$O$_9$, which has exhibited remarkable electrochemical

performances and small volume change (near-zero for LIBs[31] and < 10% for SIBs[32]). In the previous works involving CaV_4O_9 anode, its lithium/sodium storage mechanisms have been systematically studied, revealing distinct energy storage mechanisms that are closely related to structural evolution pathways. Encouraged by these works, CaV_4O_9 is also expected to be a viable anode material for use in PIBs, but there are no relevant reports so far. Therefore, its fundamental reaction mechanisms associated with structural evolution and reaction kinetics still remain inexplicit when used in PIBs.

In this work, the potential of porous CaV_4O_9 nanobelts (NBs) as a PIB anode material was carefully explored by using in situ transmission electron microscopy (TEM) approach[33−36] to observe electrochemical potassiation and depotassiation behaviors at the nanoscale. The combined use of high-resolution imaging, electron diffraction (ED), electron energy loss spectroscopy (EELS) and in situ, X-ray diffraction (XRD) enables real-time tracking of morphological/structural changes and chemical states of CaV_4O_9 NB anodes during (de)potassiation. The in situ measurements show that the initial CaV_4O_9 phase was converted into a polyphase state of V_4O_7, CaO, and K_2O phases upon potassiation, accompanied by the disappearance of cavities in the NBs. Impressively, the potassiated products could be partially converted back to the initial CaV_4O_9 phase only with some residual VO_2 phase. This partial reversibility is in sharp contrast to the completely irreversible electrochemical reactions occurring in lithium and sodium storage in CaV_4O_9, indicating their different phase evolution pathways. Remarkably, the porous morphology of NBs was restored after depotassiation. The alternately disappearing and appearing cavities in NBs were considered to effectively alleviate the drastic volume change induced by the inflow and outflow of large K ions, which can ensure good cycling stability. Rigorous electrochemical tests show that CaV_4O_9 as PIB anodes can maintain a high capacity above 125 mAh g$^{−1}$ after 150 cycles at a current density of 100 mA g$^{−1}$, exhibiting good cycling stability and great potential for potassium storage.

2. Results and Discussion

The crystal structure and morphology of the as-synthesized material were first characterized carefully, **Figure 1**. The XRD result in Figure 1a shows that the as-synthesized material is the pure CaV_4O_9 phase (JCPDS: 01-070-4469, space group: $P4/nZ$, $a = b = 8.327$ Å, $c = 5.013$ Å). Structurally, CaV_4O_9 possesses a layered structure along the c direction with Ca^{2+} distributed uniformly in the layers, as illustrated by atomic structure models in Figure 1b,c. Figure 1d shows a low-magnification TEM image of the CaV_4O_9 sample. By coupling with SEM observation in the inset of Figure 1d, the sample is confirmed to exhibit 1D porous belt-like shape with 100−200 nm in width and several microns in length, respectively. Further magnified TEM image in Figure 1e clearly shows the porous feature exhibiting many irregular cavities distributed on the CaV_4O_9 NB. The formation of such cavities is attributed to the evaporation of crystal water during synthesis.[32] Nonetheless, the NB possesses a single-crystalline nature, as proven by the corresponding single-crystalline ED pattern in the inset of Figure 1e. Figure 1f shows a high-resolution TEM image in which the lattice fringe spacings of 2.40 and 1.91 Å can be indexed as (−102) and (222) planes

of CaV_4O_9. The corresponding fast Fourier transformation (FFT) pattern in the inset of Figure 1f matches well with the tetragonal-structured CaV_4O_9. Note that the CaV_4O_9 NB was relatively stable even under prolonged electron beam irradiation and no visible structural damage appeared, as shown in Figure S1, Supporting Information. High-angle annular dark-field (HAADF) scanning transmission electron microscopy (STEM) imaging coupled with energy dispersive X-ray spectroscopy (EDS) elemental mapping was used to analyze compositional distribution. Figure 1g shows the uniform distribution of Ca, V, and O elements on individual CaV_4O_9 NBs. Additional HAADF-STEM and HRTEM characterizations further identify the successful synthesis of single-crystalline NBs of tetragonal-structured CaV_4O_9, Figure S2, Supporting Information.

To ascertain the underlying potassium storage mechanisms of CaV_4O_9 NBs during the entire electrochemical potassiation and depotassiation process, an all-solid K-CaV_4O_9 nanobattery was constructed in situ inside a TEM, as schematically illustrated in **Figure 2a**. By applying a potential of −3.0 V to the NB electrode with respect to the K counter electrode, the potassiation process was initiated. The time-sequenced TEM snapshots of the morphological evolution of individual CaV_4O_9 NBs during potassiation were recorded, as presented in Figure 2b–f (see also Movie S1, Supporting Information). During initial potassiation, K$^+$ is transported into the NB starting from its point of contact with the K resource, accompanied by the observable volume and contrast variations. Meanwhile, the cavities on the NB gradually disappear as the volume of the NB expands. Such a potassiation process can be visualized by the moveable "reaction front" (RF, marked with red arrows in Figure 2c–e) that was used to distinguish the reacted and unreacted regions.

The cross-section variation is measured with an expansion from 247 to 298 nm after full potassiation (750 s) in Figure 2f, corresponding to a ≈20.6% width expansion. In addition, the longitudinal elongation of an NB before and after potassiation can also be estimated quantitatively, Figure 2g,h. Based on the reference position, the longitudinal elongation of the NB is found to be from 499 to 523 nm after potassiation, indicating a longitudinal expansion of 4.8%. At the same time, a width expansion of 19.5% (from 221 to 264 nm) is estimated for the potassiated NB in.Figure 2g,h, implying the same degree of potassiation as the NB in Figure 2b−f The HAADF-STEM imaging and corresponding STEM-EDS element mapping further highlight the RF in a partially potassiated NB shown in Figure 2i, in which the distribution of K$^+$ gradually decreases from right to left and stops at the RF. Furthermore, the statistical results of the cross-section expansion of six NBs are shown in Figure 2j and their cross-section expansion ratios are similar (≈20%±3%). Undoubtedly, such morphological changes should result from electrochemical potassiation rather than beam-induced phase decomposition, as evidenced by additional in situ experiments in Figure S3 in Supporting Information. Further observation of the morphological details during potassiation of CaV_4O_9 NBs is carried out by focusing on the magnified TEM images, as presented in Figure 2k. As the potassiation progressed, the original cavities on the NBs were gradually filled and became smaller until they were invisible. This scenario is particularly obvious before and after the RF, as shown in Figure S4, Supporting Information. The schematic diagram in Figure 2l vividly depicts the cavity evolution of a porous CaV_4O_9
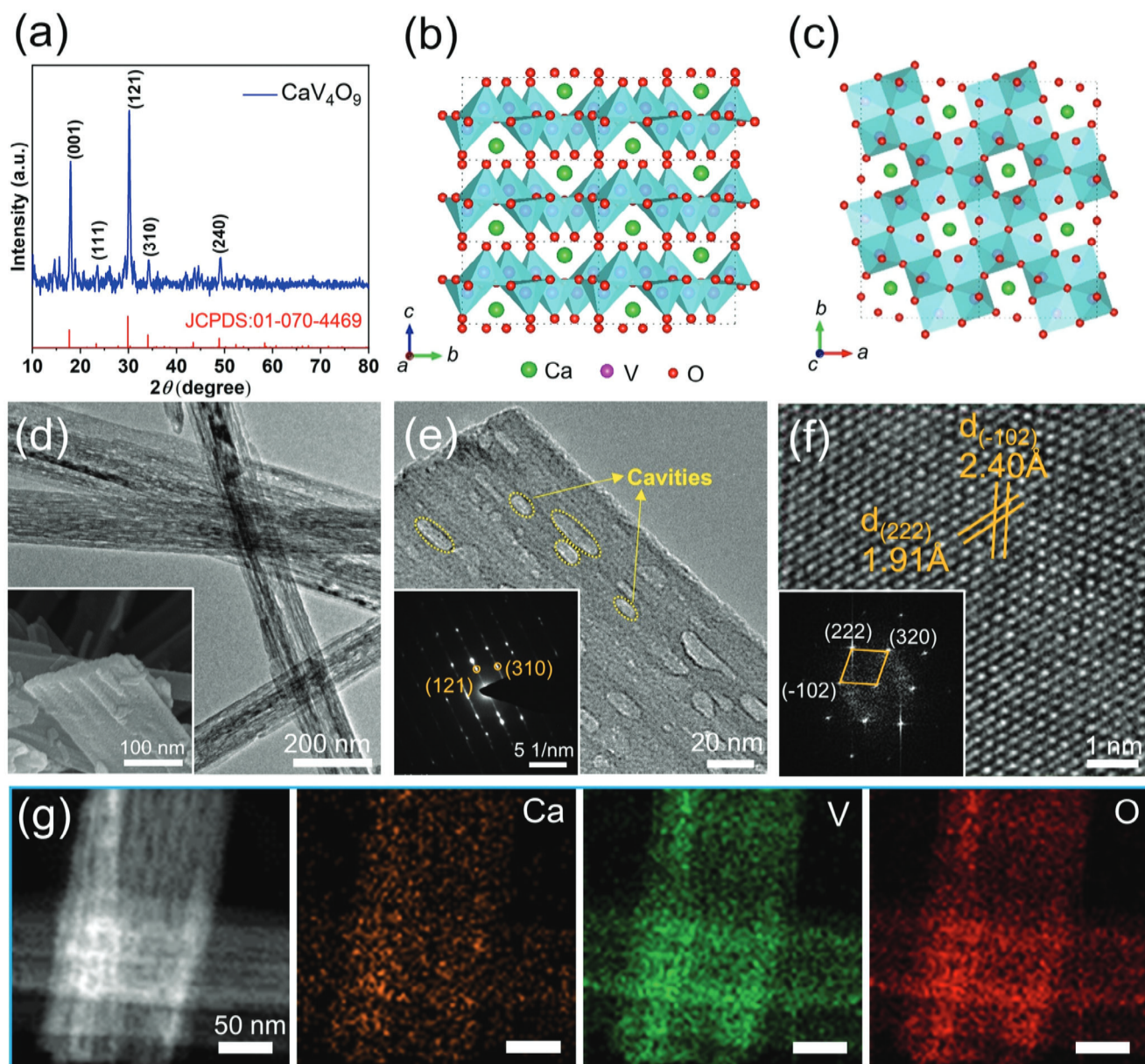
Figure 1. a) XRD pattern of the as-prepared CaV_4O_9 sample. b,c) Crystal structure models were observed along the a and c axes of CaV_4O_9, respectively. The green and red balls represent Ca and O ions, respectively, and the blue polyhedrals represent the V–O pyramids. d) Low-magnification TEM image of the CaV_4O_9 NBs with an inset of SEM image. e) High-magnification TEM image and corresponding ED pattern. f) HRTEM image and corresponding FFT pattern. g) EDS elemental maps of CaV_4O_9 NBs.

NB upon potassiation. Interestingly, this dynamic process of cavity disappearance has not been observed before for the lithiation and sodiation of CaV_4O_9 NBs,[31,32] possibly due to the larger ion size of K^+ compared to Li^+ and Na^+.

To deeply understand the overall reaction mechanism during potassiation of a single CaV_4O_9 NB, the real-time potassiation scenario is schematically illustrated in **Figure 3a,b**. Figure 3c–e shows the time-sequenced ED patterns collected in the order of K^+ concentration from low to high along the regions marked in Figure 3a,b. The pristine part on a partially potassiated NB clearly shows the single-crystalline ED pattern (Figure 3c), in which the diffraction spots marked by the orange dotted rings

can be indexed as the (111) and (121) planes of the tetragonal CaV_4O_9 phase (JCPDS: 01-070-4469). Upon a slight potassiation, the diffraction spots belonging to the original CaV_4O_9 phase basically remained, but new diffraction rings corresponding to CaO (JCPDS No. 01–1160), K_2O (JCPDS No. 26–1327), and V_4O_7 (JCPDS No. 72–1718) phases appeared, as shown in Figure 3d. Upon a deep potassiation, the CaV_4O_9 phase completely disappeared and the diffraction intensity of the CaO, K_2O, and V_4O_7 phases became stronger, but no new phases were generated, Figure 3e. Obviously, the finally potassiated products were in a polyphase state including CaO, K_2O, and V_4O_7 phases. Local HRTEM image and corresponding FFT pattern from the fully
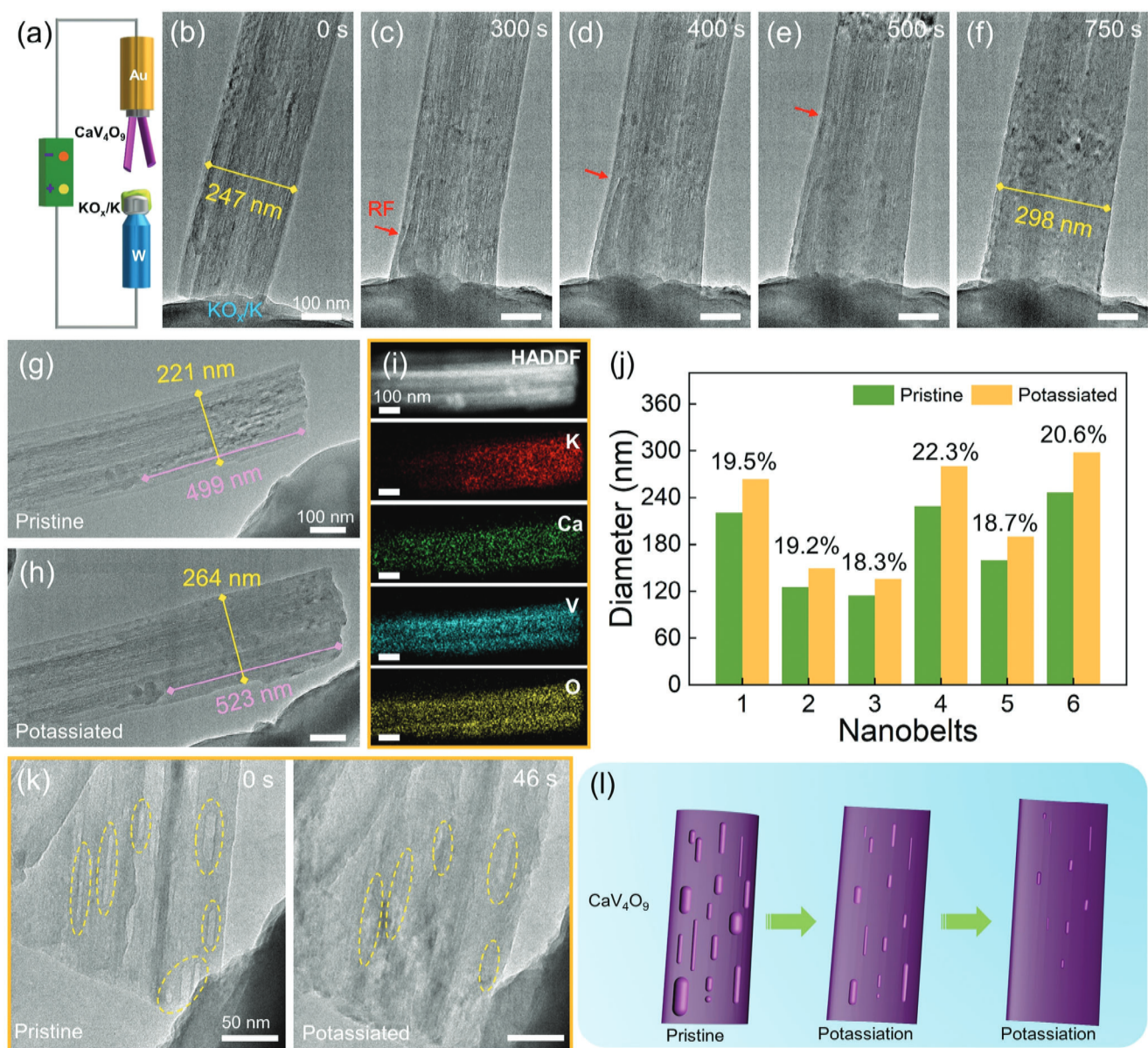
Figure 2. (a) Schematic illustration of the experimental setup for in situ electrochemical potassiation/depotassiation. b−f) and g,h) Snapshots of different CaV_4O_9 NBs during the potassiation process. i) STEM-HAADF image and EDS maps of K, Ca, V, and O at the corresponding area in the partially potassiated CaV_4O_9 NBs from (h). j) The histogram shows the variation in cross-sectional diameter of the six CaV_4O_9 NBs before and after potassiation. k) TEM images show the pristine and potassiated morphologies of a CaV_4O_9 NB. Large amounts of cavities distributed on the NB disappear during potassiation. l) Schematic illustration of morphological evolution during the first potassiation process of CaV_4O_9 NB.

potassiated region are shown in Figure 3f. Lattice fringes with d-spacing of 3.02 and 2.86 Å attributable to (004) and (−122) planes of V_4O_7 can be identified. Note that no clear lattice fringes corresponding to CaO can be detected by HRTEM, possibly due to the very small size of the CaO crystallites. It is generally recognized that although Ca ions are electrochemically inactive, they are expected to form nano-sized CaO crystallites that can result in a "spectator effect" to buffer the large volume change of electrode materials and restrain the agglomeration of active components.[37] The phase evolution of CaV_4O_9 anode during the first potassiation process is schematically given in Figure 3g.

For a deeper understanding of phase evolution pathways during potassiation of CaV_4O_9, electron energy loss spectroscopy (EELS) was also performed along the direction of K^+ diffusion on a partially potassiated NB, Figure 3h−j. The HAADF-STEM image of the partially potassiated NB and the corresponding K elemental distribution mapping is shown in Figure 3i. The increased intensity of $K-L_{2,3}$ edge is clearly observed as the potassiation progressed, Figure 3h, implying different degrees of potassiation along the longitudinal axis of NB. Moreover, a shift of the $V-L_{2,3}$ edge is observed clearly with potassiation, indicating a decrease in the valence of vanadium. As seen in Figure 3j,
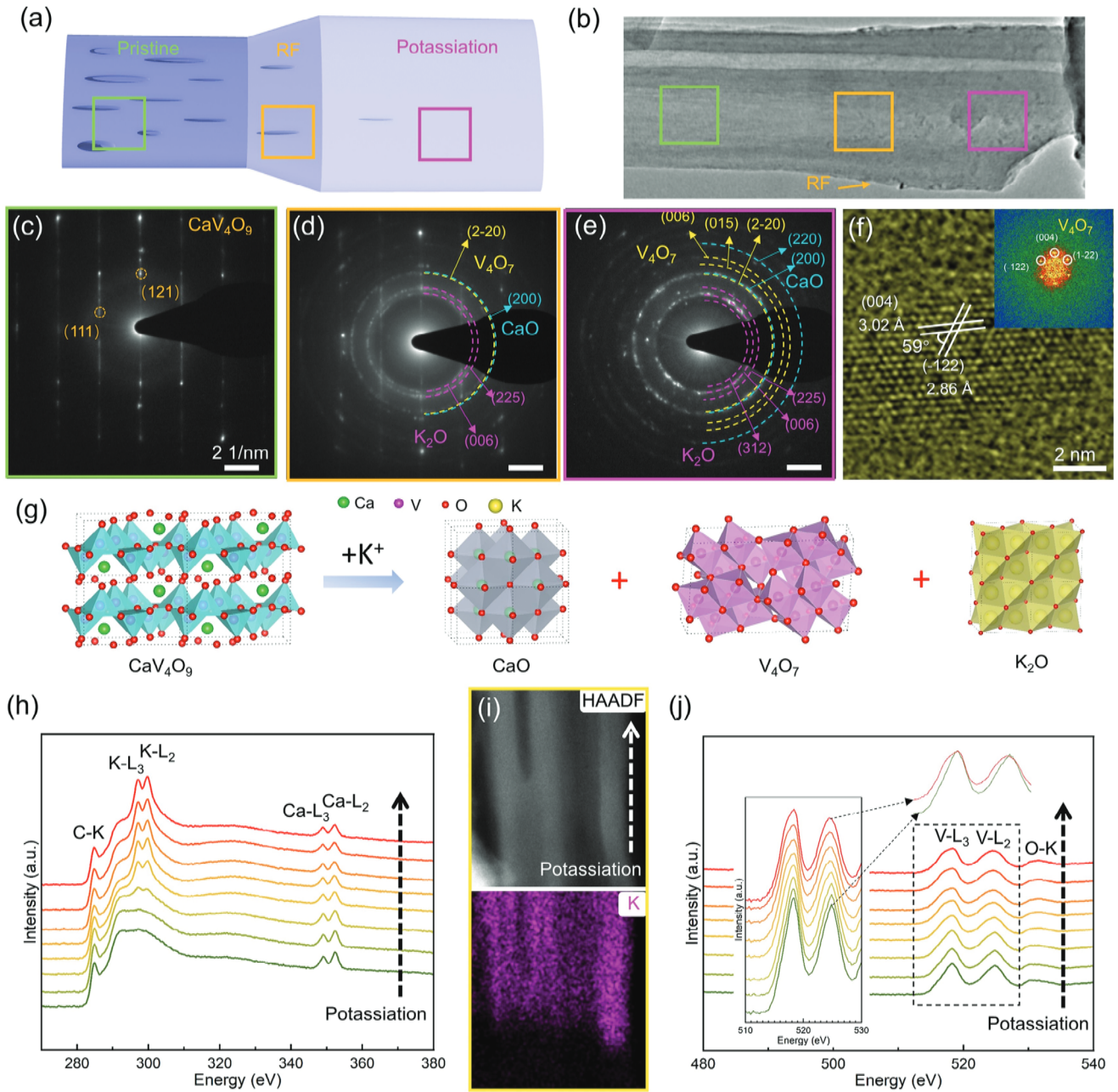
Figure 3. a) Schematic illustration of the real-time potassiation scenario. b) TEM image of the partially potassiated CaV_4O_9 NB. (c−e) ED patterns are used for identifying the phase evolution during the first electrochemical potassiation process. (f) HRTEM image of the potassiated product. g) Schematic illustration of the reaction mechanism of the CaV_4O_9 during the first potassiation process. h−j) Arranged STEM-EELS data in the order of K^+ concentration, collected from the partially potassiated NBs, the HAADF-STEM image, and the distribution of element K as shown in (i). h) K-L, Ca-L, and C-K edges. (j) V−L and O−K edges. Inset refers to the enlarged V−L edges from the pristine and fully potassiated regions.

the V L_2 and O K edges are very close; thus, defining the position of the L_2 edge on the continuum becomes difficult. Generally speaking, the L_3 edge onset energies show a monotonic increase with the cation oxidation state. The enlarged view of the V-$L_{2,3}$ peaks shows that the half-peak width of the V L_3 edge in the potassiated region is larger than that in the unpotassiated region, which indicates a clear tendency to shift to the left. Although the valence state change of vanadium dur-

ing the first potassiation process is too small (only 0.5) to quantify in the EELS data, we can clearly observe the downtrend of the valence state. It can be estimated that four moles of V^{4+} in one mole of CaV_4O_9 can be converted to four moles of $V^{3.5+}$ in one mole of V_4O_7, so two moles of electrons are transferred and the corresponding capacity is 138 mAh g^{-1}. This value is close to electrochemical testing results (which will be discussed below).
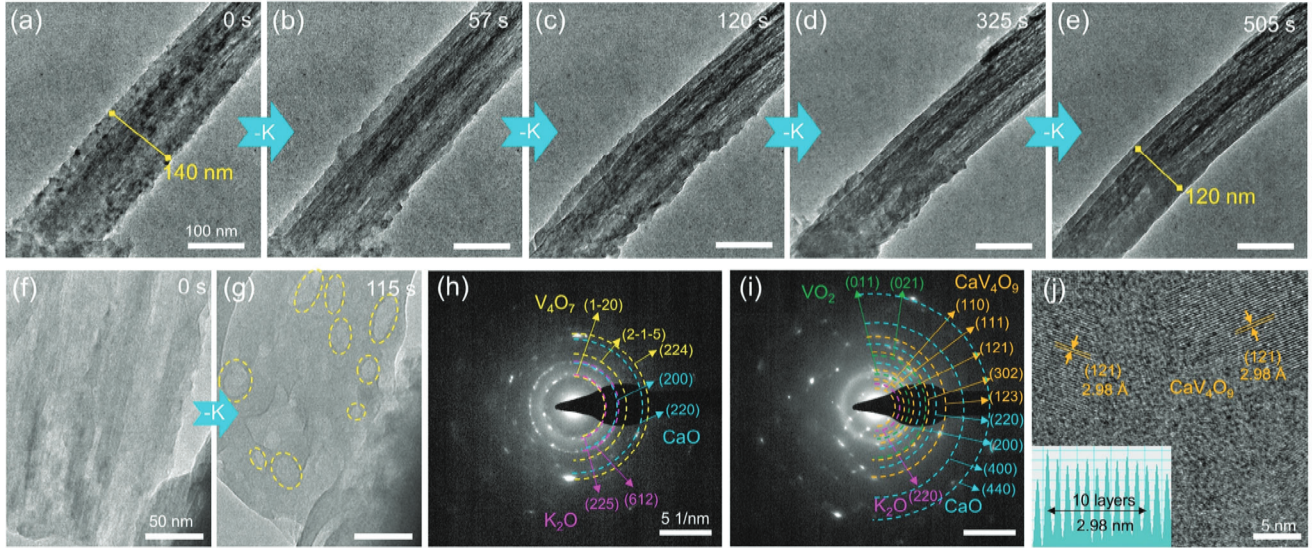
Figure 4. a–e) Time-resolved TEM images showing the morphological evolution of a CaV_4O_9 NB during the first depotassiation. f–g) TEM images show the potassiated and depotassiated morphologies of a CaV_4O_9 NB. Showing large amounts of cavities distributed on the NB reappear during depotassiation process. h–i) ED patterns used for identifying phase evolutions upon the first depotassiation process of CaV_4O_9 NB. j) HRTEM image demonstrating the depotassiated products includes the original CaV_4O_9.

To evaluate the reversibility of the potassium storage in CaV_4O_9 NBs, a constant potential of 3.0 V was applied to already potassiated CaV_4O_9 NBs to extract K ions, as typically shown in Figure 4a–e (see also Movie S2, Supporting Information) in which a NB was undergoing a typical depotassiation process. With the extraction of K^+, the diameter of the potassiated NB in **Figure** 4a–e gradually shrunk from 140 to 120 nm, corresponding to a diameter reduction of 14.3%. Impressively, the disappeared cavities in potassiation reappeared with depotassiation. The depotassiation of another NB in Figure 4f and g also resulted in the reappearance of the cavities. Note that no structural collapse in the depotassiating NBs was observed despite the fast outflow of K^+. A previous study on the failure mechanism of SnO_2 anode for SIBs revealed that nanopore formation during desodiation of SnO_2 nanowires greatly increased the electrical impedance and thus led to the poor cyclability of SnO_2 anode. However, for the CaV_4O_9 NB anode, the recovered cavities during depotassiation were congenital, and thus their reappearance did not cause a structural degradation of the NBs. In a like manner, the congenital cavities can also buffer drastic stress accumulation and volume expansion induced by the inserted K^+ during potassiation, thus avoiding the occurrence of cracking and fracture in NBs.

The ED patterns during depotassiation of NB anodes were recorded to further analyze the cycling reversibility associated with phase transformations, as displayed in Figure 4h,i. With depotassiation, the diffraction rings attributable to V_4O_7 and K_2O phases began to weaken and gradually disappeared. The original CaV_4O_9 phase was recovered as the finally depotassiated product. But, some residual VO_2 (JCPDS No. 09–0142), CaO and K_2O phases still existed in the depotassiated NB, implying an incomplete depotassiation. Figure 4j further displays a local HRTEM image of the fully depotassiated region, in which the nanograins with ordered lattice fringes can be identified as the tetragonal CaV_4O_9 phase. Obviously, the single-crystalline CaV_4O_9 NB can-

not be recovered and instead, the poly-crystalline CaV_4O_9 NB anode with the partially residual VO_2, CaO, and K_2O phases was formed after the first potassiation and depotassiation cycle.

Since the cavities on CaV_4O_9 NBs can buffer drastic stress accumulation and volume change during the first potassiation and depotassiation cycle, the cycled NBs are also expected to well run during the following cycles. To this end, further validation experiments were carried out to investigate the long-term restorability of porous CaV_4O_9 NBs. Figure 5a–i (see also Movie S3, Supporting Information) shows a typical example during the initial four cycles of a single NB with the red arrows indicating the direction of K^+ diffusion. As expected, the NB during multiple cycles can withstand the repeated volume expansion and contraction and no obvious cracking or fracture occurred in the NB, implying its good mechanical flexibility when used as the PIB anode material. **Figure** 5j further displays the cross-section expansion and contraction rates for each cycle. Notably, the NB after five cycles shows a nearly similar size as that of the initial state. While for each cycle, the disappeared cavities upon potassiation can reformed on the NB during depotassiation. However, we also found that as the number of cycles increased, fewer and fewer cavities could be recovered on the NB. This detailed observation indicates that the structural integrity of the NB anode during cycling was kept at the sacrifice of cavities. The above in situ observations demonstrate the good stability of CaV_4O_9 NB anodes during the electrochemical cycles.

The in situ ED patterns acquired from the first and fifth (de)potassiation cycles were used to examine the reversible phase transformation during multiple cycles, Figure 5k–n. As expected, the fifth cycle exhibited the same phase transformation as that in the first cycle, that is, the fully potassiated products (CaO, K_2O, and V_4O_7 phases) were partially converted into the CaV_4O_9 after each potassiation process. Similarly, the VO_2 phase and irreversible CaO and K_2O phases coexisted with the CaV_4O_9
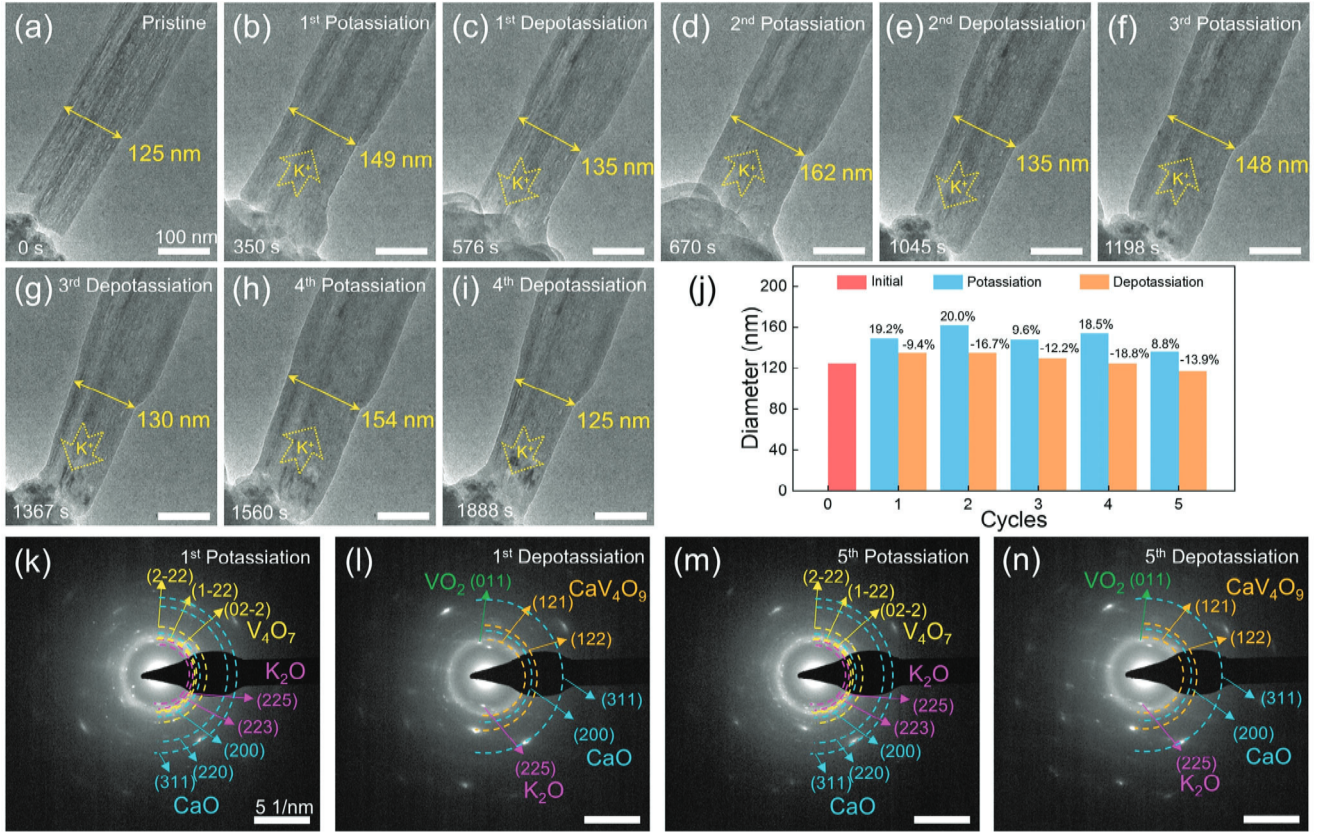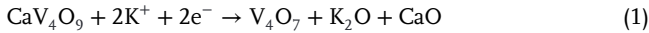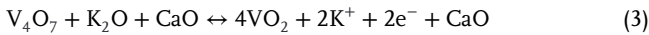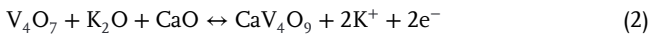
Figure 5. a−i) In situ TEM observation of the morphological evolution of CaV_4O_9 NBs electrode during the first four (de)potassiation cycles. The NBs exhibits multicycle reversible volume expansion and contraction with the insertion and extraction of potassium ions. j) Statistics of the cross-sectional diameter changes versus the number of (de)potassiation cycles. k−n) ED patterns show structural evolutions during the first two cycles of (de)potassiation processes CaV_4O_9 NB.

phase after each depotassiation. Although the starting phases during the first and fifth potassiation processes were different, the potassiated products (Figure 5k,m) were the same. Moreover, the fifth depotassiation products in Figure 5n also exhibit the same ED pattern as that of the first depotassiation product. According to the in situ measurements, no metallic substances such as V were formed during cycles. To summarize, the overall electrochemical reactions related to the partial reversible potassium storage can be expressed as follows:
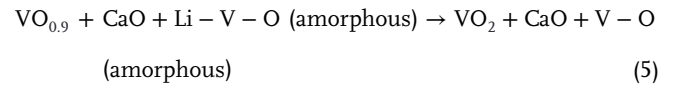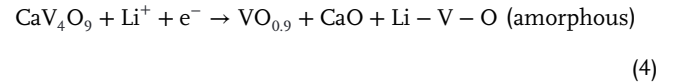
The first potassiation process:

$$CaV_4O_9 + 2K^+ + 2e^- \rightarrow V_4O_7 + K_2O + CaO \tag{1}$$

The first depotassiation process and subsequent cycles:

$$V_4O_7 + K_2O + CaO \leftrightarrow CaV_4O_9 + 2K^+ + 2e^- \tag{2}$$

$$V_4O_7 + K_2O + CaO \leftrightarrow 4VO_2 + 2K^+ + 2e^- + CaO \tag{3}$$

In addition, the electrochemical reactions of Li and Na storages in CaV_4O_9 are also provided for comparison according to the previous reports.[31,32] It is found that a common product is the newly formed CaO nanograins that can provide a self-preserving effect to prevent the agglomeration of active components in electrodes, and thus help to keep the high electrode cycling reversibility.[37] For the lithiation and sodiation, CaV_4O_9 anodes are reduced to

$VO_{0.9}$ + Li-V-O (amorphous) and $NaVO_2$ respectively and no alkali metal oxides (Li_2O and Na_2O) are formed, which is different from the potassiated products (V_4O_7 + K_2O). By comparison, the lithiated products ($VO_{0.9}$ and Li-V-O) have the lowest valence state of V and the potassiated products exhibit the highest valence state of V. In this regard, the small valence state variation of V in K storage of CaV_4O_9 anode can ensure moderate electrochemical reactions, despite the sacrifice of the capacity.

The first lithiation/delithiation process[31]:

$$CaV_4O_9 + Li^+ + e^- \rightarrow VO_{0.9} + CaO + Li - V - O \text{ (amorphous)} \tag{4}$$

$$VO_{0.9} + CaO + Li - V - O \text{ (amorphous)} \rightarrow VO_2 + CaO + V - O \text{ (amorphous)} \tag{5}$$

The first sodiation/desodiation process and subsequent cycles[32]:

$$CaV_4O_9 + 4Na^+ + 4e^- \rightarrow 4NaVO_2 + CaO \tag{6}$$

$$NaVO_2 + CaO \leftrightarrow VO_2 + CaO + Na^+ + e^- \tag{7}$$
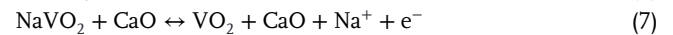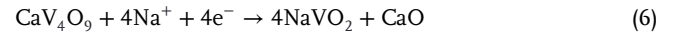
Electrochemical tests were further carried out to evaluate the potassium storage performance of CaV_4O_9 anodes. The
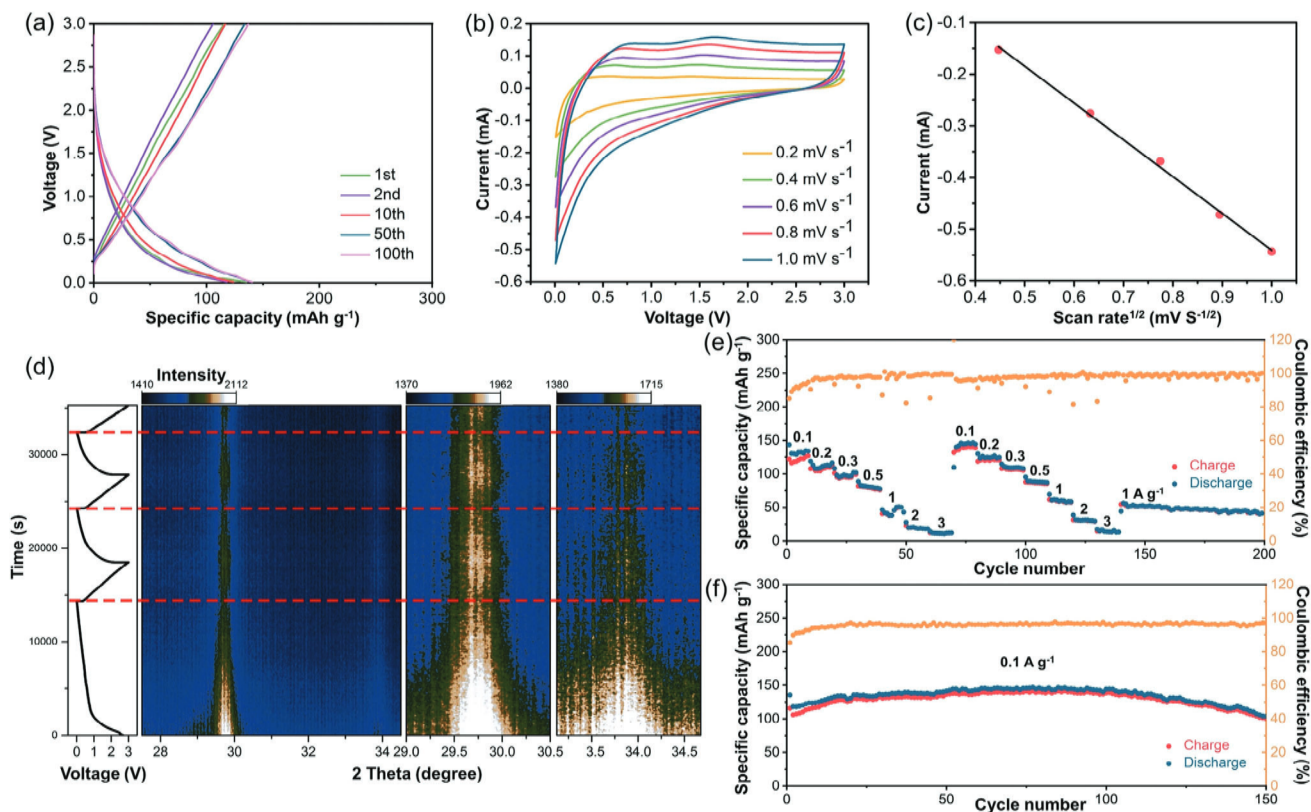
Figure 6. a) Galvanostatic discharge/charge profiles at a current density of 100 mA g^{-1} b) CV curves of CaV$_4$O$_9$ at the scan rate from 0.2 to 1.0 mV s^{-1}. c) The relation between the square root of the scan rate ($v^{1/2}$) and the corresponding currents at 0.01 V. d) In situ XRD patterns of CaV$_4$O$_9$ during the first three electrochemical cycles and the corresponding discharge/charge profiles. e)Rate performances of CaV$_4$O$_9$ at different current densities of 100, 200, 300, 500, 1000, 2000, and 3000 mA g^{-1}. f) Cycling performances and Coulombic efficiency of CaV$_4$O$_9$ at a current density of 100 mA g^{-1}.

galvanostatic discharge/charge profiles (**Figure 6a**) at 100 mA g^{-1} between 0.01 and 3V (vs. K/K$^+$) exhibit a stable capacity of ≈142 mAh g^{-1}. Compared with the storage capacities of Li and Na in CaV$_4$O$_9$ anodes,[31,32] this value is a little low due possibly to larger K$^+$ radius that causes the sluggish diffusion kinetics. In addition, no distinct voltage plateau is observed and this phenomenon also appears in other vanadate-based anode materials, such as Co$_3$V$_2$O$_8$ and NiV$_3$O$_8$.[38,39] Figure S5a shows the CV curves without obvious peaks, which are consistent with the discharge/charge profiles. The activation process could be seen in the initial scans and the capacity loss below 0.5 V is found, which could be possibly attributed to the formation of solid electrolyte interphase and side reactions at low voltages.[40,41] To clarify the K storage mechanism, CV measurements were performed at different scan rates, as displayed in Figure 6b. The potassiation currents at 0.01 V show a linear relation with the square root of the scan rate ($v^{1/2}$) (Figure 6c), which indicates a diffusion-controlled charge storage mechanism in CaV$_4$O$_9$ rather than a capacitive process.[42,43] Moreover, the reversible phase transformation was proved by in situ X-ray diffraction (XRD) measurement in Figure 6d. Although the signals detected by the in situ XRD are weak, the periodic change of diffraction peaks can be observed. During the potassiation process, the diffraction peaks at 29.9 degree and 34.0 degree corresponding to (121) and (310) planes of CaV$_4$O$_9$ phase became weak gradually, suggesting

the decomposition of CaV$_4$O$_9$ with the insertion of K$^+$. As for the depotassiation process, such peaks reappeared and gradually became strong, indicating the recovery of CaV$_4$O$_9$ phase.

The rate capability of CaV$_4$O$_9$ NB anodes was further analyzed at various current densities, Figure 6e. With increasing the current densities from 100 to 3000 mA g^{-1}, the discharge capacity decreased from 142.5 to 10.9 mAh g^{-1}. When cycled back to 100 mA g^{-1}, a reversible capacity of 142.2 mAh g^{-1} was recovered. Even for the second circulation from 100 to 3000 mA g^{-1} and then back to 1000 mA g^{-1}, such a good capacity recovery was also achieved. Corresponding discharge/charge profiles are shown in Figure S5b. Figure 6f displays the long-term cyclability of CaV$_4$O$_9$ NB anodes and corresponding Coulombic efficiency at 100 mA g^{-1}. It is found that a gradual capacity increase was observed during the initial dozens of cycles and the highest capacity reached ≈147 mAh g^{-1}. After 100 cycles, the capacity began to decrease but still remained above 100 mAh g^{-1}. In addition, the Coulombic efficiency significantly increased during the initial twenty cycles and then stabilized at ≈96% in the subsequent cycles.

It should be noted that the electrochemical potassium storage performance of the CaV$_4$O$_9$ material has never been investigated before. In the previous studies, the CaV$_4$O$_9$ NBs used as anode materials for LIBs and SIBs exhibited small or even "near-zero" volume change and remarkable electrochemical

performances.[31,32] The electrochemical tests in this work also show the huge potential of CaV_4O_9 NB anodes for PIBs. For the volume change, the complete potassiation of CaV_4O_9 based on Equation (1) results in a theoretical volume expansion of 36.6%, namely, one mole of CaV_4O_9 (173.8 Å^3) can be converted into one mole V_4O_7 (55.2 Å^3), one mole of K_2O (155.6 Å^3), and one mole of CaO (27.6 Å^3). In addition, the larger size of K^+ would lead to large interlayer expansion/contraction with insertion/extraction of K^+. However, as a matter of fact, the volume expansion of the NBs during potassiation is slightly below 36.6%, as estimated according to the in situ TEM measurements in Figure 2. This is because the unique multi-cavity morphology of CaV_4O_9 NBs can effectively offset the volume expansion induced by the inserted K^+. Moreover, according to the in situ TEM observations, the cavities on CaV_4O_9 NBs can be recovered after each depotassiation, which ensures small volume expansion for the next potassiation; as a result, the excellent electrochemical cycling stability can be maintained during discharge-charge cycles.

3. Conclusion

In summary, the morphology evolution and phase transformation pathways of CaV_4O_9 NB anodes during (de)potassiation cycles have been carefully explored by in situ TEM and in situ XRD for the first time. The results show that the original CaV_4O_9 NBs completely transform into a mixture of V_4O_7, CaO, and K_2O. Moreover, the original CaV_4O_9 phase and some residual VO_2 phase are found in the depotassiated product, indicating that the CaV_4O_9 anodes undergo a partially reversible phase transformation during cycles. In particular, the cavities on NBs disappeared during potassiation and then reappeared during depotassiation. Both the recovered morphology of cavities and the partially reversible phase transformation reactions during multiple (de)potassiation cycles contribute to good cycling stability. The direct comparisons among Li, Na, and K storage mechanisms are also discussed, highlighting the critical effect of different alkali metal ions in CaV_4O_9 anodes on the electrochemical reactions. This work provided a paradigm by revisiting the existing anode materials in lithium/sodium-ion batteries to seek out viable anodes for next-generation PIBs.

4. Experimental Section

Material Synthesis and Characterization: The CaV_4O_9 NBs were prepared by a hydrothermal method. In brief, 2 mmol of V_2O_5 was dissolved in 30 mL of deionized water and then 5 mL of H_2O_2 (30%) was added to form an orange solution after stirring for 20 min. Afterward, 90 mmol of $CaCl_2$ was added to the orange solution to form a red suspension after stirring for 2 h. The final suspension was transferred in a 50 mL Teflon-lined stainless-steel autoclave. The autoclave was sealed and heated to 200 °C for 48 h and then cooled to room temperature. The obtained product was dispersed in 30 mL of deionized water, washed with deionized water four times, and rinsed with ethanol once. After drying at 70 °C for 24 h, the sample was annealed in an H_2/Ar (5/95 volume ratio) atmosphere at 450 °C for 8 h with a heating rate of 2 °C min^{-1}. Structural characterization of the as-prepared sample was conducted using a Bruker D8 Discover X-ray diffractometer (XRD) with Cu Kα radiation source. In situ, XRD signals were obtained with the electrode covered by an X-ray-apparent beryllium sheet. Morphological characterization was carried out using a scanning electron microscope (SEM, JSM-7600F, JEOL, Japan) operated at 15 kV.

TEM imaging and ED pattern were recorded using an aberration-corrected FEI Titan 80–300 kV TEM. High-angle annular dark-field (HAADF) scanning transmission electron microscopy (STEM) imaging coupled with energy dispersive X-ray spectroscopy (EDS) elemental mapping was used to analyze compositional distribution.

In Situ TEM Electrochemical Potassiation and Depotassiation: The aberration-corrected TEM (FEI Tian 80–300 kV) with a fast-responding charge-coupled device (CCD) camera was used for in situ observation of the electrochemical reactions of CaV_4O_9 NBs, including real-time imaging, consecutive ED sampling, and energy dispersive X-ray spectroscopy (EDS) mapping. The CaV_4O_9 NBs, which were dispersed in ethanol and dropped onto a carbon film-supported TEM half-grid, were used as the electrode. Potassium metal, which was scraped onto a tungsten probe, was employed as the counter electrode and potassium source. The holder was quickly transferred into the TEM column from an Ar gas-filled sealing bag. A thin layer of KO_x, which would naturally form on the surface of the potassium metal due to the exposure of the specimen holder to air, acted as a solid electrolyte for transporting potassium ions. Then, the tungsten tip was driven by a piezo-positioner in a STM-TEM (PicoFemto) holder inside TEM to make the K/KO_x and CaV_4O_9 NBs contact. Once the contact was made, an electric bias was applied to drive the K ions to insert or extract from the NBs and thus enable electrochemical potassiation and depotassiation reactions that could be recorded in situ for subsequent analysis. In situ electron energy loss spectroscopy (EELS) studies were performed using a double aberration-corrected Thermo Fisher Themis Z S/TEM operated at 300 kV, equipped with the high-speed K3 camera.

Electrochemical Measurements: The electrochemical performance of CaV_4O_9 NB electrodes was evaluated using an assembly of 2016-type coin cells in a glove box filled with pure argon gas. The electrodes were prepared from a mixed slurry with a weight ratio of 70% CaV_4O_9 active material, 20% acetylene black, and 10% carboxy methyl cellulose (CMC aqueous solution). The mixed slurry was pasted on copper foil and dried in an oven at 70 °C for 12 h. Then, a metallic potassium foil was used both as a reference and counter electrode. A Whatman glass microfiber filter membrane acted as a separator and a solution of 0.8 M KPF_6 in ethylene carbon (EC) and diethyl carbonate (DEC) (1:1 by volume) was used as the electrolyte. Galvanostatic discharge-charge testing was performed after the activation of the first cycle at a potential range of 0.01–3 V vs. K/K^+ using a multichannel battery testing system (LAND CT2001A). Cyclic voltammetry (CV) was tested with an electrochemical workstation (CHI 760E).

Conflict of Interest

The authors declare no conflict of interest.

Author Contributions

Y.W. and P.W. contributed equally to this work. Y.W. and F.X. conducted in situ experiments and wrote this manuscript. All authors participated in the discussion and data analysis.

Data Availability Statement

Keywords

[1]   D. Larcher, J.-M. Tarascon, *Nat. Chem.* **2015**, *7*, 19.
[2]   B. Dunn, H. Kamath, J.-M. Tarascon, *Science* **2011**, *334*, 928.
[3]   Y.-K. Sun, *ACS Energy Lett.* **2019**, *4*, 1042.
[4]   C.-X. Zu, H. Li, *Energy Environ. Sci.* **2011**, *4*, 2614.
[5]   S.-W. Kim, D.-H. Seo, X. Ma, G. Ceder, K. Kang, *Adv. Energy Mater.* **2012**, *2*, 710.
[6]   Y. Fang, L. Xiao, X. Ai, Y. Cao, H. Yang, *Adv. Mater.* **2015**, *27*, 5895.
[7]   M. D. Slater, D. Kim, E. Lee, C. S. Johnson, *Adv. Funct. Mater.* **2013**, *23*, 947.
[8]   X. Xiang, K. Zhang, J. Chen, *Adv. Mater.* **2015**, *27*, 5343.
[9]   L. Wang, Y. Lu, J. Liu, M. Xu, J. Cheng, D. Zhang, J. B. Goodenough, *Angew. Chem., Int. Ed.* **2013**, *125*, 2018.
[10] Z. Jian, W. Luo, X. Ji, *J. Am. Chem. Soc.* **2015**, *137*, 11566.
[11] A. Eftekhari, Z. Jian, X. Ji, *ACS Appl. Mater. Interfaces* **2017**, *9*, 4404.
[12] Y. Cheng, Z. Yao, Q. Zhang, J. Chen, W. Ye, S. Zhou, H. Liu, M.-S. Wang, *Adv. Funct. Mater.* **2020**, *30*, 2005417.
[13] B. Ji, F. Zhang, N. Wu, Y. Tang, *Adv. Energy Mater.* **2017**, *7*, 1700920.
[14] K. Lei, F. Li, C. Mu, J. Wang, Q. Zhao, C. Chen, J. Chen, *Energy Environ. Sci.* **2017**, *10*, 552.
[15] M. Okoshi, Y. Yamada, S. Komaba, A. Yamada, H. Nakai, *J. Electrochem. Soc.* **2017**, *164*, A54.
[16] B. Yang, J. Chen, L. Liu, P. Ma, B. Liu, J. Lang, Y. Tang, X. Yan, *Energy Storage Mater.* **2019**, *23*, 522.
[17] Q. Zhang, Z. Wang, S. Zhang, T. Zhou, J. Mao, Z. Guo, *Electrochem. Energy Rev.* **2018**, *1*, 625.
[18] Z. Wang, K. Dong, D. Wang, S. Luo, Y. Liu, Q. Wang, Y. Zhang, A. Hao, C. Shi, N. Zhao, *J. Mater. Chem. A* **2019**, *7*, 14309.
[19] C. Yang, J. Feng, F. Lv, J. Zhou, C. Lin, K. Wang, Y. Zhang, Y. Yang, W. Wang, J. Li, S. Guo, *Adv. Mater.* **2018**, *30*, 1800036.
[20] H. Li, Z. Cheng, Q. Zhang, A. Natan, Y. Yang, D. Cao, H. Zhu, *Nano Lett.* **2018**, *18*, 7407.
[21] A. Eftekhari, *J. Power Sources* **2004**, *126*, 221.
[22] Y. Dong, Y. Xu, W. Li, Q. Fu, M. Wu, E. Manske, J. Kröger, Y. Lei, *Small* **2019**, *15*, 1900497.
[23] S. Chong, Y. Wu, C. Liu, Y. Chen, S. Guo, Y. Liu, G. Cao, *Nano Energy* **2018**, *54*, 106.
[24] J. Zheng, Y. Yang, X. Fan, G. Ji, X. Ji, H. Wang, S. Hou, M. R. Zachariah, C. Wang, *Energy Environ. Sci.* **2019**, *12*, 615.
[25] Y. Wu, S. Hu, R. Xu, J. Wang, Z. Peng, Q. Zhang, Y. Yu, *Nano Lett.* **2019**, *19*, 1351.
[26] Q. Zhang, J. Mao, W. K. Pang, T. Zheng, V. Sencadas, Y. Chen, Y. Liu, Z. Guo, *Adv. Energy Mater.* **2018**, *8*, 1703288.
[27] W. Zhang, W. K. Pang, V. Sencadas, Z. Guo, *Joule* **2018**, *2*, 1534.
[28] O. B. Chae, J. Kim, I. Park, H. Jeong, J. H. Ku, J. H. Ryu, K. Kang, S. M. Oh, *Chem. Mater.* **2014**, *26*, 5874.
[29] X. Xu, P. Wu, Q. Li, W. Yang, X. Zhang, X. Wang, J. Meng, C. Niu, L. Mai, *Nano Energy* **2018**, *50*, 606.
[30] V. Augustyn, B. Dunn, *Electrochim. Acta* **2013**, *88*, 530.
[31] P. Wu, X. Xu, Y. Wu, F. Xu, X. Wang, J. Meng, C. Han, X. Liu, Z. Zhu, L. Mai, *Adv. Energy Mater.* **2021**, *11*, 2003612.
[32] X. Xu, C. Niu, M. Duan, X. Wang, L. Huang, J. Wang, L. Pu, W. Ren, C. Shi, J. Meng, B. Song, L. Mai, *Nat. Commun.* **2017**, *8*, 460.
[33] J. Y. Huang, L. Zhong, C. M. Wang, J. P. Sullivan, W. Xu, L. Q. Zhang, S. X. Mao, N. S. Hudak, X. H. Liu, A. Subramanian, H. Fan, L. Qi, A. Kushima, J. Li, *Science* **2010**, *330*, 1515.
[34] Y. Wu, X. Xu, C. Zhu, P. Liu, S. Yang, H. L. Xin, R. Cai, L. Yao, M. Nie, S. Lei, P. Gao, L. Sun, L. Mai, F. Xu, *ACS Energy Lett.* **2019**, *4*, 2081.
[35] F. L. Wu, Q. Meng, M. Kaltak, J. Huang, J. L. Durham, M. Fernandez-Serra, L. Sun, A. C. Marschilok, E. S. Takeuchi, K. J. Takeuchi, M. S. Hybertsen, Y. Zhu, *Nat. Commun.* **2017**, *8*, 15400.
[36] Y. Wu, W. Luo, P. Gao, C. Zhu, X. Hu, K. Qu, J. Chen, Y. Wang, L. Sun, L. Mai, F. Xu, *Nano Energy* **2020**, *77*, 105299.
[37] M. V. Reddy, G. V. Subba Rao, B. V. R. Chowdari, *Chem. Rev.* **2013**, *113*, 5364.
[38] G. Yang, H. Cui, G. Yang, C. Wang, *ACS Nano* **2014**, *8*, 4474.
[39] S. Ni, J. Ma, J. Zhang, X. Yang, L. Zhang, *Chem. Commun.* **2015**, *51*, 5880.
[40] P. Poizot, S. Laruelle, S. Grugeon, L. Dupont, J.-M. Tarascon, *Nature* **2000**, *407*, 496.
[41] Y.-Y. Hu, Z. Liu, K.-W. Nam, O. J. Borkiewicz, J. Cheng, X. Hua, M. T. Dunstan, X. Yu, K. M. Wiaderek, L.-S. Du, K. W. Chapman, P. J. Chupas, X.-Q. Yang, C. P. Grey, *Nat. Mater.* **2013**, *12*, 1130.
[42] T. Brezesinski, J. Wang, S. H. Tolbert, B. Dunn, *Nat. Mater.* **2010**, *9*, 146.
[43] V. Augustyn, J. Come, M. A. Lowe, J. W. Kim, P.-L. Taberna, S. H. Tolbert, H. D. Abruña, P. Simon, B. Dunn, *Nat. Mater.* **2013**, *12*, 518.